Seismic Performance of Precast Shear Wall with Sleeves Connection Based on Experimental and Numerical Studies

Guoshan Xu[1,2,*,†], Zhen Wang[1,2], Bin Wu [1,2], Oreste S. Bursi [3], Xiaojing Tan [4], Qingbo Yang [5] and Long Wen[1,2]

[1] Key Lab of Structures Dynamic Behavior and Control of the Ministry of Education (Harbin Institute of Technology), Harbin, 150090, China;

[2] School of Civil Engineering, Harbin Institute of Technology, Harbin, 150090, China;

[3] Department of Civil, Environment & Mechanical Engineering, University of Trento – Italy, Trento, 38123, Italy;

[4] Yunnan Institute of building Research, Kunming, 650223, China;

[5] Jiangsu Power Design Institute Co., Ltd. of China Energy Engineering Group, Nanjing, 211102, China.

SUMMARY

The seismic behavior of a full-scale precast reinforced concrete shear wall (PRCSW) endowed with single-row grout-filled sleeves connection, which was developed for six-story precast box-modularized structures with reinforced concrete shear walls (PBSRCSWs), is investigated in this paper. In order to accurately reproduce the axial-flexure-shear boundary conditions of PRCSW specimens under quasi-static loading, this paper proposes a force-displacement mixed control method. Relevant experimental results showed that desired axial forces, rotations and lateral deformations were effectively accomplished on the specimens. Moreover, the PRCSW specimen resembled the cast-in-situ shear wall specimen in terms of failure modes, interstory drift angle, ultimate force, ductility and dissipated hysteretic energy. In particular, the maximum interstory drift angle of the PRCSW specimen reached 17.86 mrad. Finally, experimental results and numerical simulations

[*] Correspondence to: Guoshan Xu, School of Civil Engineering, Harbin Institute of Technology, Harbin 150090, China.

[†] Email address: xuguoshan@hit.edu.cn.

indicated that the proposed grout-filled sleeves connection method can be safely employed in six-story PBSRCSWs.

KEY WORDS: Precast reinforced concrete shear wall; grout-filled sleeves connection; force-displacement mixed control; quasi-static test; axial-flexure-shear boundary condition.

1. INTRODUCTION

1.1 Background and Motivation

Precast concrete structures have been studied worldwide because of their superior concrete quality and higher speed of construction compared with cast-in-situ concrete structures. Previous research on seismic precast structures goes back to the PREcast Seismic Structural Systems Research Program in the early 1990s [1]. Existing research related to precast concrete structures mainly focused on seismic performance of components/structures as well as on joint connection methods among components[2,3,4].

The use of unbonded post-tensioned precast concrete walls as the primary lateral load resisting system in seismic zones has been investigated in several studies. Hutchinson *el al*. [5] presented the results of nine prototype specimens tested to investigate the behavior and capacity of post-tensioned horizontal connections for precast concrete load bearing shear wall panels subjected to monotonic shear loading. Soudki *et al*. [6,7] studied the behavior of some horizontal connections and new innovative configurations that are believed to enhance the ductility and/or energy dissipation capacity for precast wall panels, and presented design considerations based on the experimental results. Kurama *et al.* [8] investigated the seismic behavior of unbonded post-tensioned precast concrete walls

and proposed a performance-based seismic design approach. Holden *et al*. [2] and Hamid and Mander [9,10,11] investigated the seismic performance of precast reinforced and prestressed concrete walls, and the walls achieved superior displacement capacity with less damage. Perez *et al*. [12] introduced a design-oriented analytical model to estimate the nonlinear lateral load behavior of unbonded post-tensioned walls, and validated the model with available experimental results. An experimental program developed to study the seismic performance of precast reinforced concrete wall panels with and without openings was carried out in Reference [13]. It was shown that precast reinforced concrete walls investigated meet the requirements of Eurocode 8, Part 1 [14] for walls designed to DCM - medium ductility- as large, lightly reinforced walls. Another extensive experimental program based on a total of twenty-eight tests was conducted within the SAFECLADDING project [15], that aimed at improving the connection systems between cladding panels and precast RC buildings in seismic-prone zones. The reliability of friction-based devices was confirmed by several tests completed without any damage. Moreover, a reduced relative displacement, combined with a load limitation within system connections, avoided either compatibility troubles experimented with the isostatic criterion as well as excessive forces of the integrated criterion.

Erkmen and Schultz [16] investigated the effects of tendon layout, tendon end-anchorage configuration and external vertical load on the self-centering ability of unbonded post-tensioned precast concrete shear walls subjected to earthquake loading. Sritharan *et al.*[17] introduced an innovative precast concrete wall system consisting of a precast wall with end columns; they combined a precast, unbonded and post-tensioned wall with two end columns using a set of special cost-effective energy dissipating connectors.

The use of precast concrete walls in seismic zones to replace monolithic cast-in-place shear walls

has been investigated in several studies. Soudki *et al.*[18] experimentally investigated five mild steel connections for a precast concrete panel wall system and concluded that both ductility and energy dissipation properties of these connections are comparable to those of monolithic connections. Kang et al. [19] proposed bonded or unbonded longitudinal rebars with partially reduced cross-sectional area to be used in the plastic hinge area. Test results revealed that gap opening and shear slip at the panel joints were prevented by using the proposed methods. Smith *et al.*[20] compared the lateral load behavior of hybrid precast concrete shear wall specimens to precast specimens designed to emulate monolithic cast-in-place shear walls; results showed the potential of precast walls in seismic regions.

The grout-filled sleeves connection represents an alternative option for precast concrete walls. Adajar et al. [21] established a new, simple and economical technique of connecting vertical bars in precast concrete shear walls. They concluded that the ultimate strength of splices used in their investigation is equal to tensile strength of the spliced bar when the lapping distance equals or exceeds 25 times the bar diameter. Belleri and Riva [22] investigated the suitability of grouted sleeve connections as column-to-foundation connections for precast concrete structures in seismic regions. Their results demonstrated that grouted sleeves could ensure similar ductility and energy dissipation capacity of structure members. Buckling of longitudinal steel bars could be prevented by the confinement provided by the grouted sleeves, and compressive strength of grout could also be improved. Henin and Morcous [23] investigated the use of non-proprietary bar splice sleeves for precast concrete construction; test results indicated that the proposed bar splice sleeves exhibited adequate capacity to fully develop reinforcing bars while being simpler to use and more economical than current proprietary splice sleeves. Cyclic performance of precast concrete shear walls with a mortar-sleeve connection for longitudinal steel bars was investigated by Peng *et al*. [24], and it was

concluded that failure mode of precast shear wall specimens was similar to that of cast-in-place shear wall specimen, including tensile yielding of longitudinal steel bars and crushing of concrete in the compressive zone.

The aforementioned investigations were mainly carried out with quasi-static tests (QSTs) under simplified axial-shear boundary conditions. Clearly, approximate boundary conditions may influence experimental results or even bias failure mode of specimens. Therefore, the seismic behavior of precast reinforced concrete shear walls (PRCSW) with grout-filled sleeves connection should be investigated by QSTs with accurate boundary condition simulation of axial-flexure-shear loads.

1.2 Scope

In view of the advantages of the use of PRCSWs over cast-in-situ concrete structures, such as their superior quality and more ease of construction, a precast box-modularized structure with reinforced concrete shear walls (PBSRCSWs) program named “A Set of Technology Study and Engineering Application Examples for Building Industrialization in Yunnan Province” was funded in China. Along this line, this paper introduces a horizontal joint connection technology characterized by a single-row grout-filled sleeves connection for PRCSWs. The QSTs of PRCSW with sleeve connection under axial-flexure-shear loads was conceived and outlined in Section 2. The test setup and a versatile force-displacement mixed control method capable of controlling both rotations, axial loads and lateral deformations boundary conditions during QSTs are presented in Section 3. Moreover, experimental observations and main results of the experimental program are summarized in Section 4, where experimental results are compared with those of a cast-in-situ shear wall specimen. In addition, Section 5 presents the FE modelling effort capable of capturing behavior of shear walls

under coupled axial-flexure-shear loads. Finally, conclusions are summarized in Section 6.

2. EXPERIMENTAL SPECIMENS

2.1 Overview of the prototype structure

This research is based on the prototype structure of a PBSRCSWs. The prototype structure is designed according to the Chinese Code for Seismic Design of Buildings [25] and was investigated to determine the seismic performance of the structure. The plan view of the relevant prototype structure is shown in Figure 1 whilst Boxes A and B in each story are depicted in Figure 2. The symbols Q, LL, GYZ, GJZ and GAZ represent the shear wall, coupling beam, wing column, corner column and hidden column, respectively, in Figure 1.

Three types of joint connections have been proposed for the six-story PBSRCSWs: i) a horizontal wall-to-wall joint connection characterized by longitudinal reinforcements spliced indirectly by single-row grout-filled sleeves; ii) a vertical wall-to-wall connection characterized by a stirrup bolted with vertical reinforcements; iii) a non-composite floor slab connection [26].This paper focuses on the performance of the horizontal wall-to-wall sleeves connection method for connecting adjacent floors of RC shear wall, and the relevant technology throughout the paper is referred to as a single-row grout-filled sleeves connection. This method entails comparably better performance in terms of low-cost and easy construction.

2.2 The specimens

Part of the PRCSWs in the first story is chosen as the specimen TW1, and one contrasting cast-in-

situ RC shear wall specimen, named SW1, is also tested. The dimensions and reinforcements for the two specimens are shown in Figure 3. The dimensions of the two full-scale specimens are 3,000 mm (Height) × 1,540 mm (Width) × 180 mm (Thickness). The dimensions of the top and bottom beams for the two specimens are 2,800 mm (Length) × 900 mm (W) × 500 mm (H).

The details of the grout-filled sleeves connection for the six-story PBSRCSWs are shown in Figure 4. The dimensions and parameters of the sleeves are shown in Figure 5 and Table 1. The quantity and diameter of the indirectly spliced steel bars for longitudinal reinforcements can be determined by the principle that the area of the spliced steel bars is equal to the area of longitudinal reinforcements inside the wall. In this paper, 10 C22 spliced steel bars are used for specimen TW1. The length of the steel bar is determined such that the steel bar meets the requirements of the Chinese Code for Design of Concrete Structures [27]. The steel bars for connecting the lower story wall are screwed into the sleeves before anchoring the sleeves at the predetermined position at the bottom central line of the wall. The corrugated pipes are then installed on both the grouting hole and vent hole of the sleeves. The steel bars for connecting the upper story wall are anchored at the predetermined position on the top central line of the wall with a sleeve connection length of 145 mm outside the wall, with the bottom beam being the same as for specimen TW1. Cement mortar of 20 mm in height is placed on the boundary of the top and bottom story.

For the contrasting specimen SW1, the shear wall is manufactured and concreted monolithically with the top and bottom beams. For the precast specimen TW1, the shear wall was shaped and concreted monolithically with the top beam, and the bottom beam was manufactured and concreted separately. Then, these two parts were assembled and connected with the proposed single-row grout-filled sleeves, as shown in Figure 6. The sleeves were fully grouted by a self-leveling grouting

material after the shear wall and bottom beam had been assembled.

2.3 Material properties

Material tests for both concrete and steel reinforcements were carried out with an MTS Universal Testing Machine at the Structural and Seismic Testing Center of Harbin Institute of Technology. Three 100-mm edged cube samples were taken from each concrete batch. The cube compressive strength f_{cu} of concrete was obtained by the measured average compressive strength with a reduction factor of 0.95 according to the Chinese Standard for Test Method of Mechanical Properties on Ordinary Concrete [28]. Relevant values for shear walls and grouting material are collected in Table 2. Also samples of steel bars for each diameter were collected and tested. The experimentally obtained corresponding measured average tensile yield strength f_y and ultimate strength f_u, are shown in Table 3.

3. TEST SETUP AND EXPERIMENTAL METHOD

3.1 Test setup

Preliminary numerical pushover analysis for the investigated prototype six-story PBSRCSWs conducted by the finite element software OpenSEES using shell elements [29], see Section 5 for further details, showed that the rotations on the top of the specimen are nearly linearly related to the lateral deformations on the top of the specimen as indicated in Figure 7; moreover, the axial loads of the shear wall changed only slightly along the wall. As a result, the boundary conditions on the top of the specimen had to be accurately simulated to boost the performance of the shear wall tests. In this respect, the three-DoF testing system at the Structural and Seismic Testing Center of Harbin Institute

of Technology was chosen as loading facility for QSTs, as depicted in Figure 8. The testing system is composed mainly of an L-shaped beam, a vertical reaction frame, a horizontal reaction wall, three servo-hydraulic actuators -numbered A, B and D in Figure 8, and the corresponding controller as well as the anchor bolts. The stroke of the three actuators is ±250 mm and the loading capacity is +2,000 kN and -1,300 kN. Actuator A was settled up horizontally to simulate the lateral deformations whilst Actuators B and D were settled up vertically to simulate both the rotations and vertical deformations at the top of the specimens. The displacement control with the amplitudes of integer times of the yield displacement was adopted for Actuator A. Because the axial loads were nearly constant on the shear wall specimens, only one constant axial load was set. Therefore, Actuators B and D should be controlled to achieve not only a constant axial load but also the foreseen rotations on the specimen tops. Thus the force-displacement mixed control method was employed.

The deformations of each specimen were monitored by 11 linear variable displacement transducers (LVDTs), as shown in Figure 9. In particular, LVDTs 1-7 were used to measure the lateral displacements in different positions of each specimen; LVDTs 8 and 9 were adopted to monitor the rotations on the top of the specimen whilst LVDTs 10 and 11 were used to monitor the vertical displacements of the bottom beam. The deformations of each specimen in the locations corresponding to the LVDTs 1-5 were defined with reference to the displacements of LVDT 7 at the bottom beam.

3.2 Experimental method

During QSTs, axial loads were typically imposed on the specimen by means of one or more jacks, whilst horizontal loads or deformations were realized by means of one or more servo-hydraulic actuators. These techniques raise two types of issues with regard to boundary conditions: i) axial loads

may not be as accurate as horizontal loads because they are accomplished by jacks; ii) the desired rotations on the specimen top cannot be accurately achieved during testing. Clearly, these issues may influence experimental results or even distort specimen failure mode. In fact, accurate boundary condition simulation and relevant actuator control methods are quite important for QSTs. As a result in recent years, several types of testing systems and/or control methods have been proposed and validated for solving different types of problems (Pan *et al.*[30] ; Nakata *et al.*[31,32]; Wang *et al.*[33]; Pan *et al.*[34]). In order to achieve an accurate control of axial loads, rotations and lateral deformations on specimens with three-DoF testing system, one novel force-displacement mixed control method is also proposed in this paper.

3.2.1 Boundary condition analysis

Figure 10 presents the horizontal, vertical and rotational deformations of a specimen under Actuators A, B and D in the three-DoF testing system presented in Subsection 3.1; in detail, d_1, d_2 and d_3 indicate the horizontal displacement response of Actuator A and the vertical displacement responses of Actuators B and D, respectively. In our case the length of Actuators B and D at the mid-stroke is about 3,623 mm, the rotations of Actuators B and D due to the deformations of Actuator A -typically less than 100 mm- are negligible. Therefore, d_2 and d_3 can be considered the displacements of Actuators B and D and can also be assumed as the displacements on the specimen corresponding to Actuators B and D. If one neglects the deformations of the L-shaped beam and defines d_0 as the vertical equilibrium position, then d_2 and d_3 can be estimated by,

$$d_2 = d_0 - \frac{L}{2}\theta \tag{1}$$

$$d_3 = d_0 + \frac{L}{2}\theta \tag{2}$$

in which L is the lateral distance between Actuators B and D, θ is the rotation at the top of the specimen, d_0 is the deformation parameter related to the axial load F and the axial stiffness K of the specimen, which can be expressed as

$$K = \frac{F}{d_0} \tag{3}$$

By substituting Equation (3) into (1) and (2), one gets:

$$\begin{Bmatrix} d_2 \\ d_3 \end{Bmatrix} = \begin{bmatrix} \frac{1}{K} & -\frac{L}{2} \\ \frac{1}{K} & \frac{L}{2} \end{bmatrix} \begin{Bmatrix} F \\ \theta \end{Bmatrix} \tag{4}$$

Equation (4) can be used to determine the desired displacements of Actuators B and D to achieve both the desired axial loads and rotations on the specimen top.

The lateral motions of the L-shaped beam induced by the rotations at the top of the specimen are negligible compared to the displacement responses d_1 of Actuator A. Therefore, only displacement responses d_1 are considered. As a result, the relationship between θ and d_1 at the top of the specimen can be obtained by,

$$\theta = \mu d_1 \tag{5}$$

where μ is a linear correlation coefficient based on the simulated results depicted in Figure 7 and further discussed in Section 5. In greater detail, μ reads 3.414×10^{-4} rad/mm.

When conducting QSTs, the desired lateral displacement d_1 and the axial load F are typically predetermined. The rotations on the top of the specimens can be calculated by Equation (5) and if L and K remain unchanged during the QSTs, Equation (4) can be directly applied to calculate desired displacements of Actuators B and D. We define this procedure as the open-loop displacement control method. Nonetheless, the axial stiffness K of the specimens might vary during a QSTs as well as the

distance L between Actuators B and D in Equation (4) or the deformations of the L-shaped beam. As a result, the aforementioned open-loop displacement control method might induce control errors on the axial loads and/or rotations on specimen tops. In order to solve this issue, a closed-loop force-displacement mixed control method is proposed hereinafter.

3.2.2 A force-displacement mixed control method

The block diagram of the general force-displacement mixed control method proposed in this paper is shown in Figure 11. The diagram is composed of two feedback control loops: one is the inner displacement feedback control loop -inner-loop- of Actuators A, B and D, and the other is the outer feedback control loop -outer-loop- of forces and rotations. In the figure, TA_1, TA_2 and TA_3 are the transfer functions of Actuators A, B and D, respectively; PI_d_1, PI_d_2 and PI_d_3 are the inner-loop proportional-integral (PI) controllers for Actuators A, B and D; PI_θ and PI_F are the outer-loop PI controllers for the rotations and axial forces at the top of the specimens; dc_1, dc_2 and dc_3 are the desired displacements of Actuators A, B and D; d_1, d_2 and d_3 are the measured displacement responses of Actuators A, B and D; F_C is the desired constant axial load, i.e. 1200 kN in these tests; F is the measured axial force imposed on the specimen as sum of forces corresponding to Actuators B and D; θ is the measured rotation imposed on the top of the specimens that is related to the responses of Actuators B and D. Both the axial stiffness K and the distance L in Equation (4) vary during a QST; thus, in order to determine the displacement commands of Actuators B and D in Figure 11, both the initial stiffness K_{ini} and the initial distance L_{ini} are used as conversion factors. The entailing errors induced by K_{ini} and/or L_{ini} are expected to be eliminated by the outer-loop controllers involving PI_F and PI_θ. They should be designed to achieve the desirable axial loads and rotations on the

specimens. Although many types of feedback controller are available, the traditional PI controller is preferred here.

3.3 Experimental method validation

QSTs were conducted on specimens SW1 and TW1 using the Three-DoF testing system presented in Subsection 3.1 combined with the force-displacement mixed control method discussed above. The designed axial load was 1390 kN and the L-shaped beam on the specimen approximately weighted 190 kN. Therefore, the vertical Actuators B and D dealt with 1,200 kN during the QSTs. With regard to the TW1 specimen, Figure 12 presents the force responses of Actuators B and D during the QST. The results indicate the effect control of the total axial force on the specimen, which is relatively stable at approximately 1,200 kN. The mean value of the control errors of the axial forces is 13.7 kN, and this value can be considered negligible compared with the desired load of 1,200 kN. The comparison between desired (or target) and measured rotations for the TW1 specimen is shown in Figure 13 and they are quite close to each other. Moreover, both the desired and measured relationships between rotations and lateral displacements of the specimen are depicted in Figure 14. As expected, the measured rotations are linearly related to the measured lateral displacements. The mean value of the control errors of the rotations reads 7.03×10^{-4} rad and is close to zero. The desired axial loads and rotations of the specimen are achieved with the proposed force-displacement mixed control method. Similar conclusions can be obtained from the experimental results of the specimen SW1. As a result, the control method entails wide application prospects for the MDoF tests of civil engineering structures. In addition, a better control accuracy can be obtained by fine tuning the controller gains of the PI controller.

4. EXPERIMENTAL RESULTS

4.1 Experimental observations

4.1.1 Observations for the SW1 specimen

The first series of cracks for the specimen SW1, i.e. the cast-in-situ RC shear wall, occurred horizontally at the bottom edge of the shear wall, see Figure 15, when the lateral displacement increased to 6 mm. When the lateral displacement reached 12 mm, a number of new horizontal cracks formed along the vertical direction of the specimen. Part of the cracks inclined along the extension and the longitudinal reinforcement on the edge of the specimen appeared to have yielded. When the lateral displacement approached 24 mm, the inclined cracks expanded rapidly, and several diagonal cracks appeared across the central line of the specimen. When the lateral displacement increased to 54 mm, the cover concrete exhibited spalling at the bottom corners and the lateral force reached its ultimate value. The test ended when the concrete at the bottom corner crushed.

4.1.2 Observations for the TW1 specimen

Similar phenomena were observed for the specimen TW1, i.e. the precast shear wall. The first series of cracks for the specimen TW1 occurred horizontally at the bottom edge of the shear wall, as shown in Figure 16, when the lateral displacement approached 6 mm. When the lateral displacement increased to 12 mm, a number of new horizontal cracks formed along the vertical direction of the specimen; the cracks inclined along the extension, and the longitudinal reinforcement on the edge of the specimen yielded. When the lateral displacement reached 24 mm, more horizontal cracks were observed, the cracks further inclined along the extension, and the horizontal cracks at the bottom of

the specimen extended and expanded rapidly. When the lateral displacement approached 48 mm, the diagonal cracks extended and expanded rapidly and the lateral force reached the ultimate value. Again, the test ended when the concrete at bottom corner crushed.

4.2 Hysteretic loops and skeleton curves

The relationship between lateral force F and lateral deformation Δ of both specimens SW1 and TW1 is shown in Figure 17 whilst the corresponding skeleton curves are depicted in Figure 18. The main parameters that characterize these curves are listed in Table 4. A careful reader can observe that the specimen TW1, i.e. the precast RC shear wall, basically behaved similarly to the specimen SW1, i.e. the cast-in-situ RC shear wall, in terms of hysteretic loops and skeleton curve. In particular, the bearing capacity of specimen SW1 decreased rapidly at failure, whereas the strength of the specimen TW1 dropped slowly. Table 4 gathers the average values of the cracking force F_{cr}, the yield force F_y and the failure –ultimate- force F_u for the specimen TW1; they are very close to those of the specimen SW1. The difference of the average values between TW1 and SW1 are about 3.1% and -10.7% for the cracking force F_{cr} and the failure –ultimate- force F_u.

4.3 Displacement and ductility of specimens

Table 5 collects the yield displacement value Δ_y, the ultimate displacement value Δ_u and the corresponding ductility factor Δ_u / Δ_y for specimens SW1 and TW1, respectively. The ultimate displacement (Δ_u) was defined as the lateral maximum displacement when the horizontal load decreased to 85% of the ultimate force (F_u) or when the specimen was heavily damaged and incapable of sustaining any more increasing horizontal load. The interstory drift angles θ, which is defined as

the interstory deformations of specimen divided by the interstory height, corresponding to the yield displacement Δ_y and ultimate displacement Δ_u are also presented in Table 5. The ductility factor of the specimen TW1 is about 55.1% greater than that of the specimen SW1, and the maximum interstory drift angle of the specimen TW1 is 17.86 mrad. This values is greater than the limiting value of 8.33 mrad established in the Chinese Code [25], indicating a relatively good deformability of the precast RC shear wall.

4.4 Stiffness characterization

The secant stiffness values which characterized the specimen behavior are gathered in Table 6 and shown in Figure 19. Clearly, the secant stiffness values corresponding to the cracked point K_{cr}, the yield point K_y, the ultimate force point K_p and the ultimate displacement point K_u decreased; moreover, similar stiffness degradation behavior can be observed for the two specimens. The difference between TW1 and SW1 are about 7.6%, -0.8% and -6.9% for cracking, the ultimate force and the ultimate displacement, respectively.

4.5 Energy dissipation behavior

The energy dissipation property of the specimens under exam is shown in Figures 20 and 21, respectively. Figure 20 presents the energy dissipation per cycle, which is defined as the area enclosed by each load-displacement hysteresis curve. The relevant energy dissipation per cycle of the two specimens increases with the increasing of lateral deformations, and the two specimens exhibit similar energy dissipation properties. Figure 21 shows the energy dissipation ratio per cycle, defined as the ratio of the area of each hysteresis loop to the area of the right-angled triangle that defines the relevant

elastic energy per cycle. The energy dissipation ratio slightly increases with the increase in the lateral deformations of each specimen, and the ratios of the two specimens nearly match each other.

5. FINITE ELEMENT ANALYSIS OF PRECAST SHEAR WALLS

5.1 FE models for shear walls

Numerical simulations of shear wall specimens were performed by means of the multi-layer shell element model suggested in Reference [29]. In order to simulate the grout-filled sleeves connections, we employed truss elements at the boundaries, as depicted in Figure 22. In particular, the sleeves and the corresponding spliced steels were simulated by means of truss elements. Thus, the truss elements provided tensile forces equivalent to C 8 steels -as shown in Table 3- inside the boundary shear wall, starting from the top of the spliced steels to the bottom beam. The concrete on the boundary region provided compression forces, in order to compensate the possible strength reduction due to concrete pouring in the bottom beam. It should be noted that the definition of the interaction and of the contact surface between elements is a key step in the implementation of the finite element model [35,36]. The interaction between steel reinforcements and concrete was modeled considering the perfect adhesion between concrete and reinforcement bars in this paper. The deformation effects of rebars were not taken into account by the model.

The material properties reported in Tables 2 and 3 and the relevant FE properties shown in Tables 7 and 8 were used in numerical simulations. In detail in Table 7, f_{cu} represents the concrete crushing strength, epsc0 defines the concrete strain at the maximum strength, epscu represents the concrete strain at the crushing strength, epstu identifies the ultimate tensile strain, and stc represents the shear retention factor. In Table 8, b represents the strain-hardening ratio whilst R0, cR1 and cR2 control the

transition from elastic to plastic branches of steel properties.

5.2 FE responses and comparisons

The simulation of force-displacement relationships for specimens SW1 and TW1 are illustrated in Figure 23. In a greater detail, Figure 23 shows that simulation results match experimental results well, indicating the effectiveness of the multi-layer shell element model suggested in Subsection 5.1. The simulations match well experimental results also for the precast RC shear wall with sleeve connections, as indicated in Figure 23. The comparison between experimental and numerical results illustrated the effectiveness of the multi-layer shell element combined with the proposed truss elements for the proper simulation of PRCSWs endowed with the sleeve connection methodology. It should be noted that the simulation model failed to capture the breakdown performance in the last cycle of the specimen SW1 test and the rapid drop off when unloading in the cycles from -30 to -60 mm range of the specimen TW1 test. Further work is necessary for improving the sufficiency of the model.

6. CONCLUSIONS

The behavior of a precast reinforced concrete shear wall (PRCSW) endowed with single-row grout-filled sleeves connection under coupled axial-flexure-shear loads was investigated in this paper by quasi-static test (QST). The force-displacement mixed control method was proposed for accurately simulating the coupled axial-flexure-shear boundary conditions of PRCSW specimens subject to QSTs. The primary conclusions are summarized herein.

Firstly, experimental results showed that axial forces, rotations and lateral deformations for

specimens subjected to quasi-static cyclic tests were effectively accomplished by the proposed force-displacement mixed control method. Therefore, it appears to have wide application prospects for MDoF coupled axial-flexure-shear loads testing of civil engineering components/structures.

Secondly, it was shown from the comparison of experimental results between the PRCSW and the cast-in-situ specimen that the former specimen behaved similarly to the cast-in-situ specimen with respect to failure mode, interstory drift angle, ultimate force, ductility, stiffness degradation and energy dissipation capacity under coupled axial-flexure-shear loads. In particular, the maximum interstory drift angle of the PRCSW specimen approached 17.86 mrad. Moreover, experimental results underlined that the proposed grout-filled sleeves connection method is suitable for six-story box-modularized PRCSWs.

Finally, the comparison between experimental and numerical results illustrated the effectiveness of the multi-layer shell element combined with the proposed truss elements for the proper simulation of PRCSWs endowed with the sleeve connection methodology.

ACKNOWLEDGMENTS

The National Key Research and Development Program of China (Grant No. 2016YFC0701106), the National Science Foundation of China (Grant No. 51308159, 51161120360 and 51408157) and A Set of Technology Study and Engineering Application Examples for Building Industrialization in Yunnan Province (2012CA025) are greatly acknowledged by the authors for supporting this study. The authors also thank Prof. Hongbin Jiang and Mr. Yunfei Ma of the Harbin Institute of Technology, for their effort in testing activities.

REFERENCES

[1] Nigel Priestley M J. Overview of PRESSS research program. *PCI Journal*, July-August, 1991; **36**(4): 50-57.

[2] Holden T, Restrepo J, Mander J B. Seismic performance of precast reinforced and prestressed concrete walls. *Journal of Structural Engineering* 2003; **129**(3): 286-296. DOI: http://dx.doi.org/10.1061/(ASCE)0733-9445(2003)129:3(286).

[3] Zoubek B, Matej F, Tatjana I. Estimation of the cyclic capacity of beam-to-column dowel connections in precast industrial buildings. *Bulletin of Earthquake Engineering* 2015; **13** (7): 2145-2168. DOI: 10.1007/s10518-014-9711-0.

[4] Magliulo G, Ercolino M, Cimmino M, Capozzi V, Manfredi G. Cyclic shear test on a dowel beam-to-column connection of precast buildings. *Earthquake and Structures* 2015; **9**(3): 541-562. DOI http://dx.doi.org/10.12989/eas.2015.9.3.541.

[5] Hutchinson R L, Rizkalla S H, Lau M, Heuvel S. Horizontal post-tensioned connections for precast concrete loadbearing shear wall panels. *PCI Journal*, November-December, 1991; **36**(6): 64-76.

[6] Soudki K A, West J S, Rizkalla S H. Seismic design considerations for precast concrete shear wall connections. *Proceedings of the 1993 Annual CSCE Conference*, Fredericton, New Brunswick. 1993.

[7] Soudki K A, Rizkalla S H, Daikiw R W. Horizontal connections for precast concrete shear walls subjected to cyclic deformations part 2: Prestressed connections. *PCI Journal* 1995; **40**(5): 82-96.

[8] Kurama Y, Pessiki S, Sause R, Lu L. Seismic behavior and design of unbonded posttensioned precast concrete walls. *PCI Journal*, May-June, 1999; **44**(3): 72-89.

[9] Hamid N H, Mander J B. Lateral seismic performance of multipanel precast hollowcore walls. *Journal of Structural Engineering* 2010; **136**(7): 795-804. DOI:

http://dx.doi.org/10.1061/(ASCE)ST.1943-541X.0000183.

[10] Hamid N H, Mander J B. A comparative seismic performance between precast hollow core walls and conventional walls using incremental dynamic analysis. *Arabian Journal for Science and Engineering* 2012; **37**(7): 1801-1815. DOI: 10.1007/s13369-012-0301-7.

[11] Hamid N H, Mander J B. Damage avoidance design for buildings. *KSCE Journal of Civil Engineering* 2014; **18**(2), 541-548. DOI: 10.1007/s12205-014-0016-2.

[12] Perez F J, Sause R, Pessiki S. Analytical and experimental lateral load behavior of unbonded posttensioned precast concrete walls. *Journal of Structural Engineering (ASCE)* 2007; **133**(11): 1531-1540. DOI: 10.1061/(ASCE)0733-9445(2007)133:11(1531).

[13] Todut C, Dan D, Stoian V. Theoretical and experimental study on precast reinforced concrete wall panels subjected to shear force, *Engineering Structures* 2014; **80**: 323-338. DOI: 10.1016/j.engstruct.2014.09.019.

[14] EN 1998-1. Eurocode 8: design of structures for earthquake resistance.

[15] Negro P and Lamperti Tornaghi M. Seismic response of precast structures with vertical cladding panels: The SAFECLADDING experimental campaign. *Engineering Structures* 2017; **132**: 205-228. DOI: 10.1016/j.engstruct.2016.11.020.

[16] Erkmen B and Schultz A E. Self-centering behavior of unbonded, post-tensioned precast concrete shear walls. *Journal of Earthquake Engineering* 2009; **13**:1047-1064. DOI: 10.1080/13632460902859136.

[17] Sritharan S, Aaleti S, Henry R S, Liu K, Tsai K. Precast concrete wall with end columns (PreWEC) for earthquake resistant design. *Earthquake Engineering & Structural Dynamics* 2015; **44**: 2075-2092. DOI: 10.1002/eqe.2576.

[18] Soudki K A, Rizkalla S H, LeBlanc B. Horizontal connections for precast concrete shear walls subjected to cyclic deformations Part 1: Mild steel connections. *PCI Journal*, July-August, 1995; **40**(4): 78-96.

[19] Kang S, Kim O, Park H. Cyclic loading test for emulative precast concrete walls with partially reduced rebar section. *Engineering Structures* 2013; **56**: 1645-1657. DOI:10.1016/j.engstruct.2013.07.036.

[20] Smith B J, Kurama Y C, McGinnis M J. Behavior of precast concrete shear walls for seismic regions: Comparison of hybrid and emulative specimens. *Journal of Structural Engineering (ASCE)* 2013; **139**(11): 1917-1927. DOI: 10.1061/(ASCE)ST.1943-541X.0000755.

[21] Adajar J, Yamaguchi T, Imai H. An experimental study on the tensile capacity of vertical bar joints in a precast shearwall. *Proceedings, Japan Concrete Institute* 1993; **15**(2): 1255-1261. (in Japanese)

[22] Belleri A, Riva P. Seismic performance and retrofit of pre-cast concrete grouted sleeve connections. *PCI Journal* 2012; **57**(1):97-109.

[23] Henin E, Morcous G. Non-proprietary bar splice sleeve for precast concrete construction. *Engineering Structures* 2015; **83**: 154-162. DOI:10.1016/j.engstruct.2014.10.045.

[24] Peng Y Y, Qian J R. Wang Y H. *Materials and Structures* 2016; **49**(6): 2455-2469. DOI:10.1617/s11527-015-0660-0.

[25] GB 50011-2010. Code for seismic design of buildings. (in Chinese)

[26] Xu G, Wang Z, Wu B, Bursi O S, Tan X, Yang Q, Wen L, Jiang H. Pseudodynamic tests with substructuring of a full-scale precast box-modularized structure made of reinforced concrete shear walls. *The Structural Design of Tall and Special Buildings* 2017; Online. DOI: 10.1002/tal.1354.

[27] GB 50010-2010. Code for design of concrete structures. (in Chinese)

[28] GB/T 50081-2002. Standard for test method of mechanical properties on ordinary concrete. (in Chinese)

[29] Lu X Z, Xie L L, Guan H, Huang Y L, Lu X. A shear wall element for nonlinear seismic analysis of super-tall buildings using OpenSees. *Finite Elements in Analysis & Design* 2015; **98**: 14-25.

http://doi.org/10.1016/j.finel.2015.01.006.

[30] Pan P, Nakashima M, Tomofuji H. Online test using displacement-force mixed control. *Earthquake Engineering & Structural Dynamics* 2005; **34**(8): 869-888. DOI: 10.1002/eqe.457.

[31] Nakata N, Spencer Jr. B F, Elnashai A S. Mixed load/displacement control strategy for hybrid simulation. *Proceedings of the 4th International Conference on Earthquake Engineering*, Taipei, Taiwan. 2006. No. 094.

[32] Nakata N, Spencer Jr. B F, Elnashai A S. Multi-dimensional hybrid simulation using a six-actuator self-reaction loading system. *The 14th World Conference on Earthquake Engineering*. October 12-17, 2008, Beijing, China.

[33] Wang T, Mosqueda G, Jacobsen A, Cortes-Delgado M. Performance evaluation of a distributed hybrid test framework to reproduce the collapse behavior of a structure. *Earthquake Engineering & Structural Dynamics* 2012; **41**(2): 295-313. DOI: 10.1002/eqe.1130.

[34] Pan P, Zhao G, Lu X, Deng K. Force-displacement mixed control for collapse tests of multistory buildings using quasi-static loading systems. *Earthquake Engineering & Structural Dynamics* 2014; **43**(2): 287-300. DOI: 10.1002/eqe.2344.

[35] Zoubek B, Fahjan Y, Fischinger M, Isakovic T. Nonlinear finite element modelling of centric dowel connections in precast buildings. *Computers and Concrete* 2014; **14**(4): 463-477. DOI: 10.12989/cac.2014.14.4.463.

[36] Magliulo G, Ercolino M, Cimmino M, Capozzi V, Manfredi G. FEM analysis of the strength of RC beam-to-column dowel connections under monotonic actions. *Construction and Building Materials* 2014; **69**: 271-284. DOI 10.1016/j.conbuildmat.2014.07.036.

TABLE CAPTIONS:

Table 1. Dimensions of sleeves (mm).

Table 2. Properties of concrete.

Table 3. Properties of steel bars.

Table 4. Main parameters of skeleton curves.

Table 5. Displacement and ductility values of specimens.

Table 6. Secant stiffness values of specimens.

Table 7. Properties of concrete used in OpenSEES.

Table 8. Properties of steel adopted in OpenSEES.

Table 1. Dimensions of sleeves (mm).

Type	L	L1	L2	D	M	D0	t
GTB4-22-A	195	68	126	48	23	32	5

Table 2. Properties of concrete.

Type	Class	No. of Samples	f_{cu}/MPa
Shear wall	C30	3	31.8
Grouting material	C60	3	70.1

Table 3. Properties of steel bars.

Type and Grade	Symbol	d/mm	No. of Samples	f_y/MPa	f_u/MPa
HRB400	C	8	3	410.3	651.9
HRB400	C	10	3	427.4	673.1
HRB400	C	16	3	455.9	607.8
HRB400	C	22	3	467.5	618.2

Table 4. Main parameters of skeleton curves.

Type	F_{cr}			F_y			F_u		
	+	-	**Average**	+	-	**Average**	+	-	**Average**
SW1	300.6	300.3	300.5	368.3	411.9	390.1	630.7	674.7	652.7
TW1	236.3	383.5	309.9	266.9	355.8	311.4	496.7	668.9	582.8

Table 5. Displacement and ductility values of specimens.

Type	Δ_y/mm (θ_y/mrad)		Δ_u/mm (θ_u/mrad)		Δ_u /Δ_y	
	+	-	+	-	+	-
SW1	9.6 (3.20)	14.7 (4.90)	56.1 (18.7)	67 (22.33)	5.8	4.6
TW1	7.9 (2.63)	4.6 (1.53)	71.6 (23.87)	53.8 (17.93)	9.1	10.9

Table 6. Secant stiffness values of specimens.

Type	K_{cr}**/(kN/mm)**	K_{y}**/(kN/mm)**	K_{p}**/(kN/mm)**	K_{u}**/(kN/mm)**
SW1	47.6	32.1	12.2	8.7
TW1	51.2	49.8	12.1	8.1

Table 7. Properties of concrete used in OpenSEES.

Type	**f_{cu}/MPa**	**epsc0**	**epscu**	**epstu**	**stc**
SW1	6.14	0.0050	0.03	0.001	0.08
TW1	6.14	0.0050	0.03	0.001	0.058

Table 8. Properties of steel adopted in OpenSEES.

Type	b	R0	cR1	cR2
SW1	0.005	13	0.925	0.15
TW1	0.005	13	0.95	0.04

FIGURE CAPTIONS:

Figure 1. Plan view of PBSRCSWs: (a) First story; (b) Other stories.

Figure 2. Models of the coupled box: (a) Box A; (b) Box B.

Figure 3. Dimensions and reinforcements: (a) The TW1 specimen; (b) The SW1 specimen.

Figure 4. Grout-filled sleeves connection for shear walls.

Figure 5. Details of a sleeve.

Figure 6. Photo of the shear wall horizontal joint connection.

Figure 7. Relationship between rotation and lateral deformation.

Figure 8. Test setup.

Figure 9. Displacement transducer layout.

Figure 10. Schematic of specimen deformation under horizontal and vertical loadings.

Figure 11. Block diagrams of the proposed force-displacement mixed control method.

Figure 12. Force responses of the vertical Actuators B and D for the TW1 specimen.

Figure 13. Comparison between target and measured rotations.

Figure 14. Relationship between rotation and lateral displacement.

Figure 15. Photo and schematic crack patterns of the specimen SW1: (a) Photo; (b) Schematic.

Figure 16. Photo and schematic crack patterns of the specimen TW1: (a) Photo; (b) Schematic.

Figure 17. Hysteretic loops: (a) Specimen SW1; (b) Specimen TW1.

Figure 18. Skeleton curves of specimens SW1 and TW1.

Figure 19. Stiffness degradation curves of specimens SW1 and TW1.

Figure 20. Energy dissipation per cycle for specimens SW1 and TW1.

Figure 21. Energy dissipation ratio per cycle for specimens SW1 and TW1.

Figure 22. FE model of a shear wall: (a) SW1; (b)TW1.

Figure 23. Comparison of hysteretic loops for specimens SW1 and TW1.

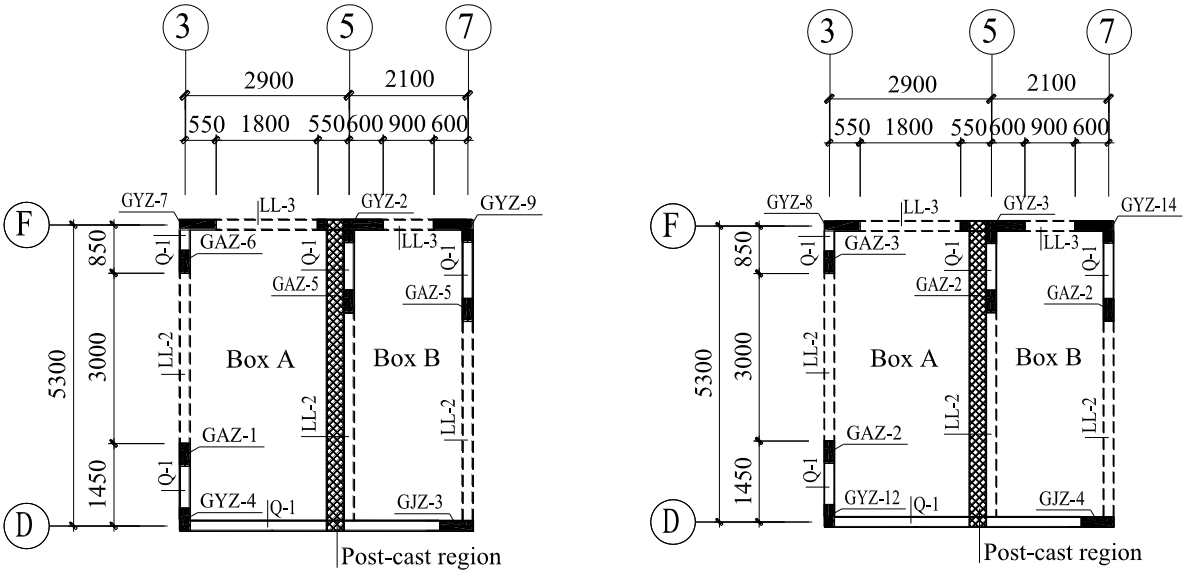

(a) First story (b) Other stories

Figure 1. Plan view of PBSRCSWs.

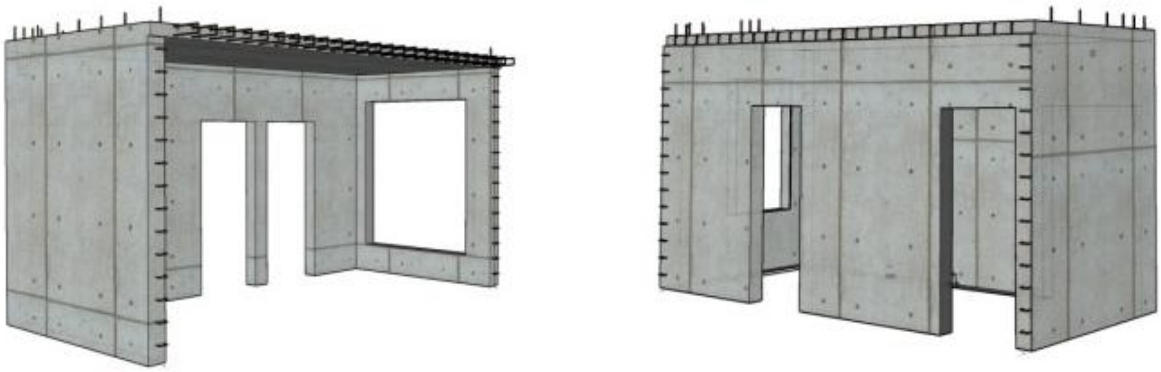

(a) Box A (b) Box B

Figure 2. Models of the coupled box.

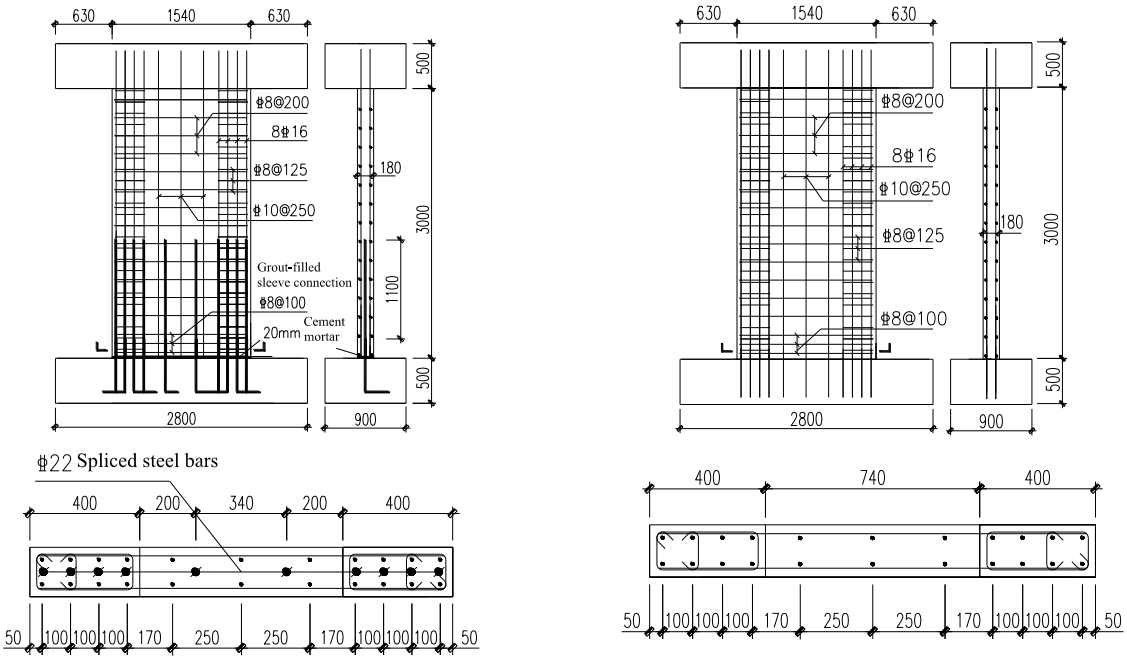

(a) The TW1 specimen (b) The SW1 specimen

Figure 3. Dimensions and reinforcements.

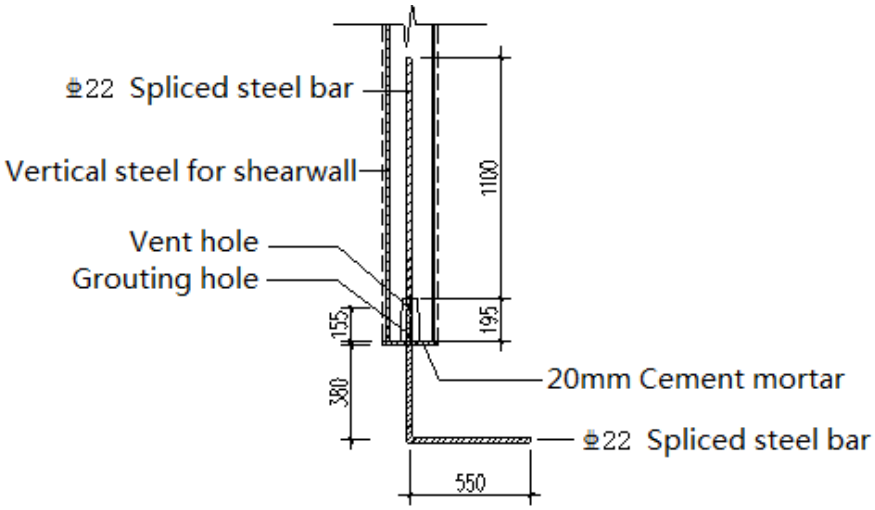

Figure 4. Grout-filled sleeves connection for shear walls.

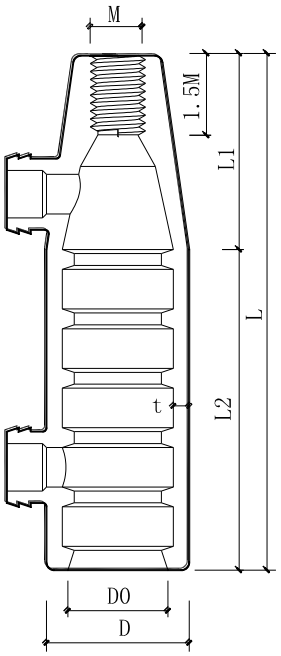

Figure 5. Details of a sleeve.

Figure 6. Photo of the shear wall horizontal joint connection.

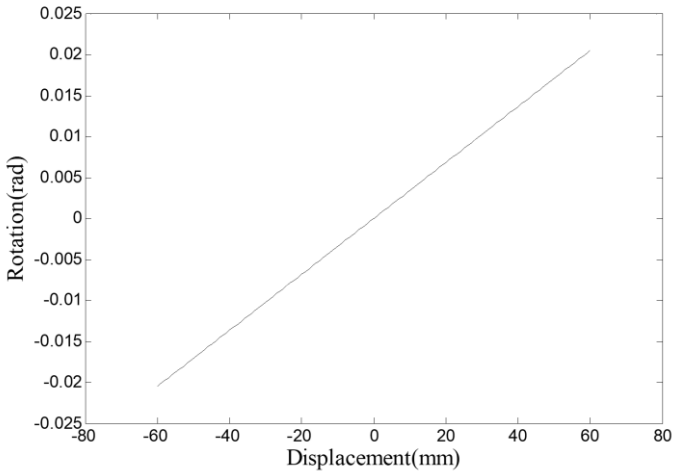

Figure 7. Relationship between rotation and lateral deformation.

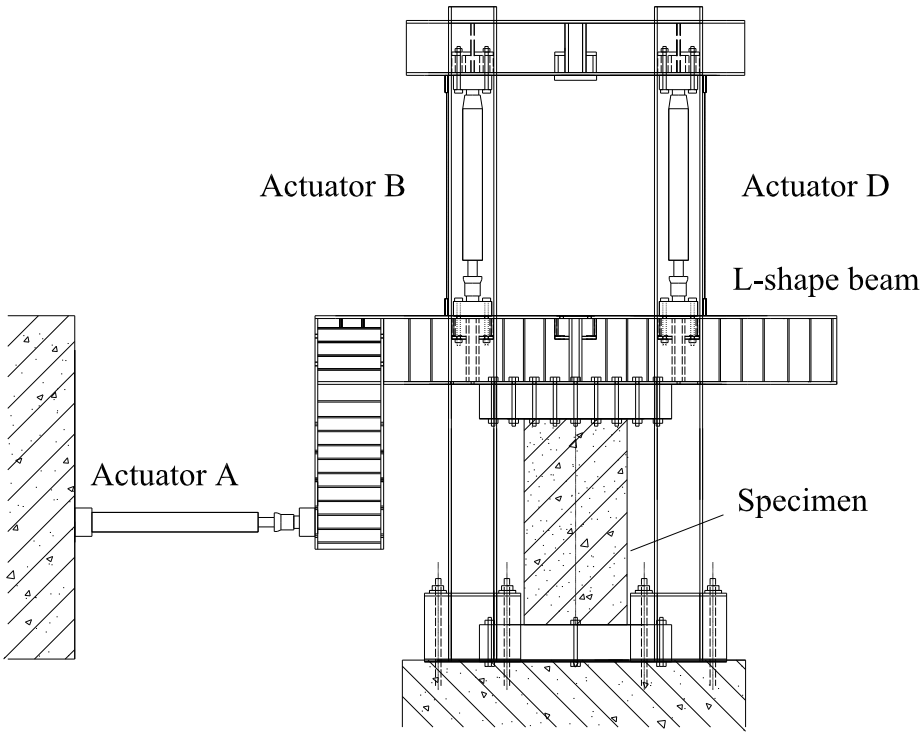

Figure 8. Test setup.

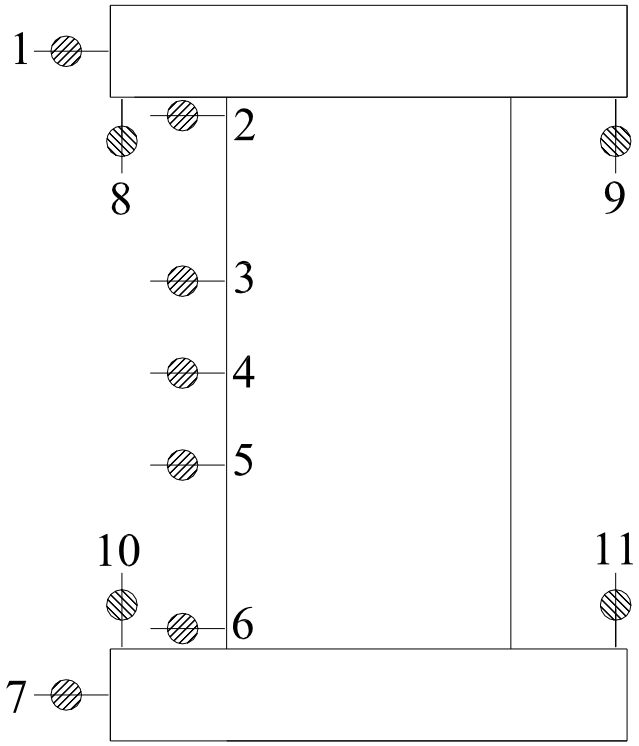

Figure 9. Displacement transducer layout.

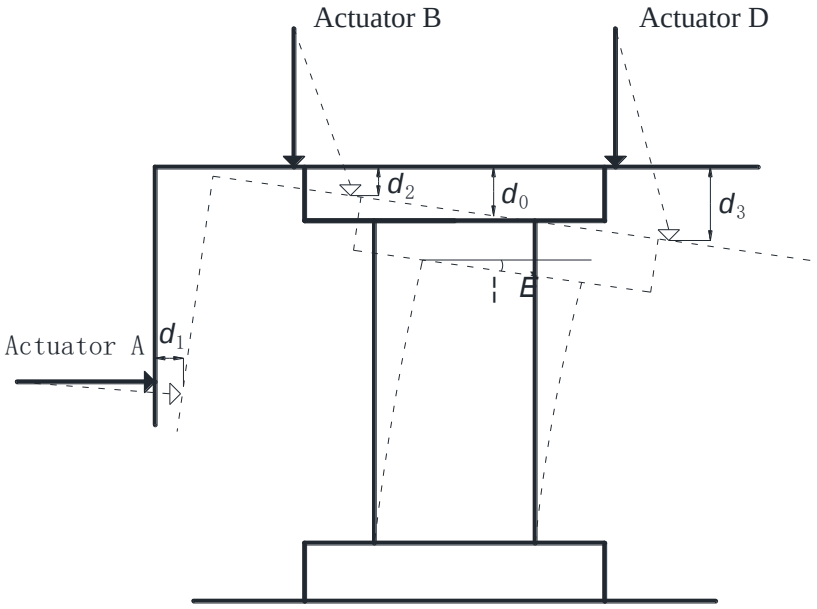

Figure 10. Schematic of specimen deformation under horizontal and vertical loadings.

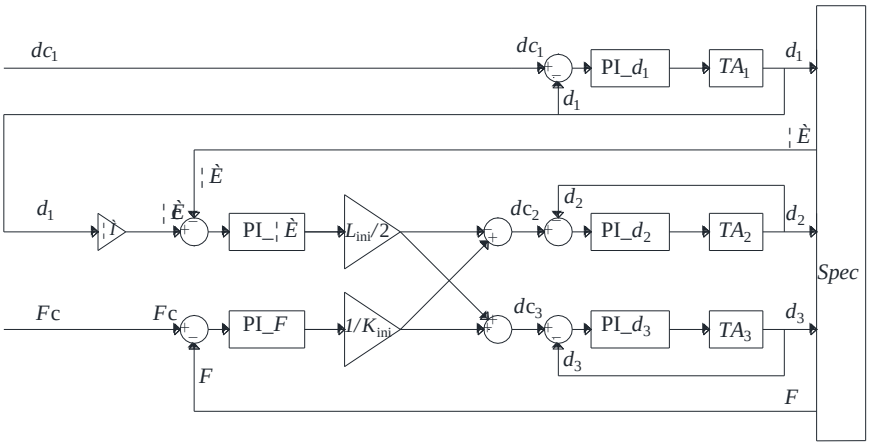

Figure 11. Block diagrams of the proposed force-displacement mixed control method.

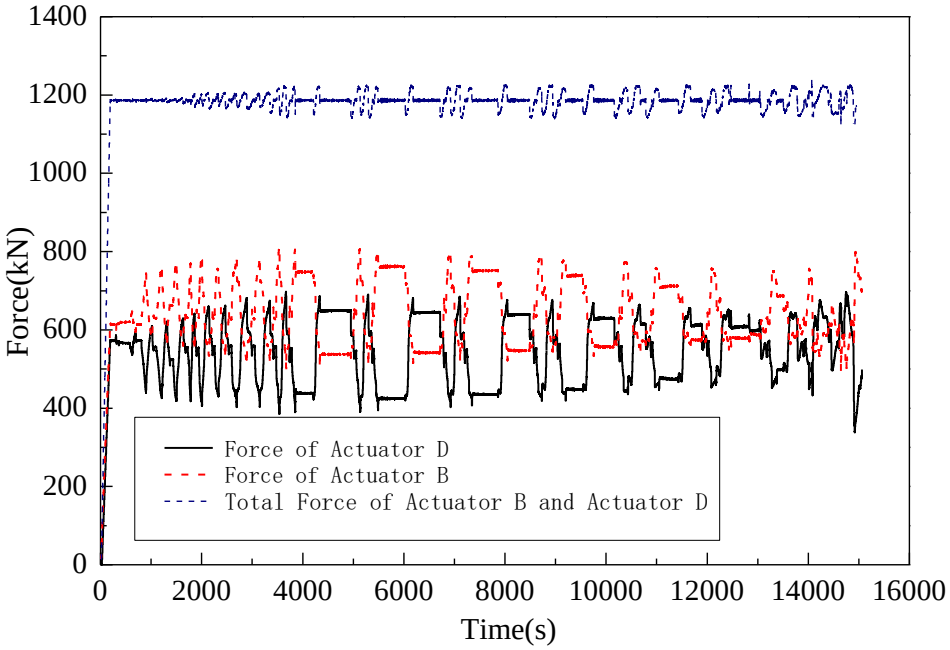

Figure 12. Force responses of the vertical Actuators B and D for the TW1 specimen.

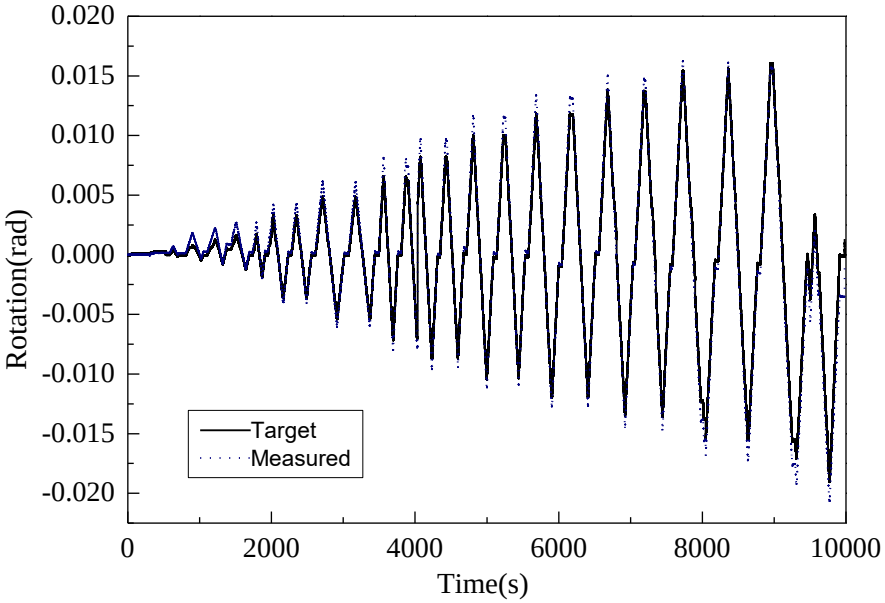

Figure 13. Comparison between target and measured rotations.

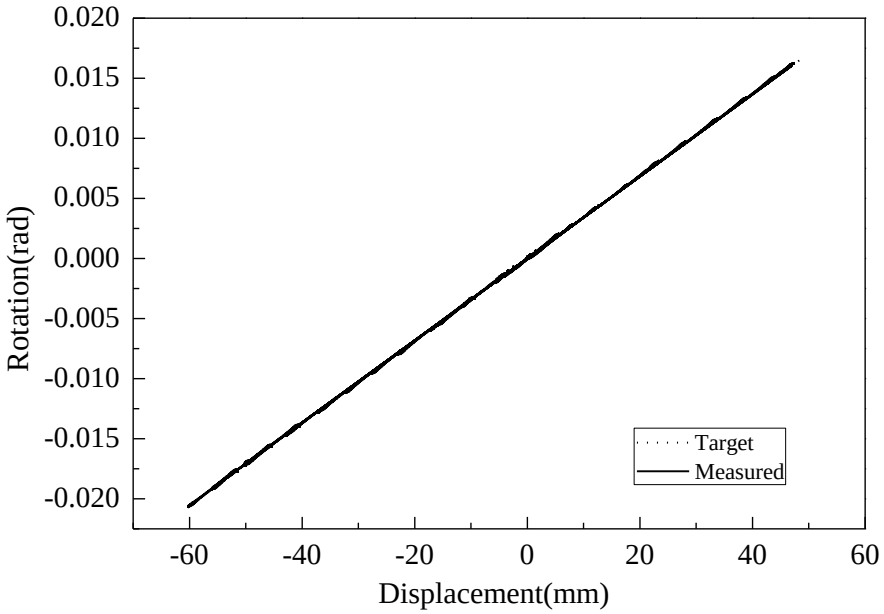

Figure 14. Relationship between rotation and lateral displacement.

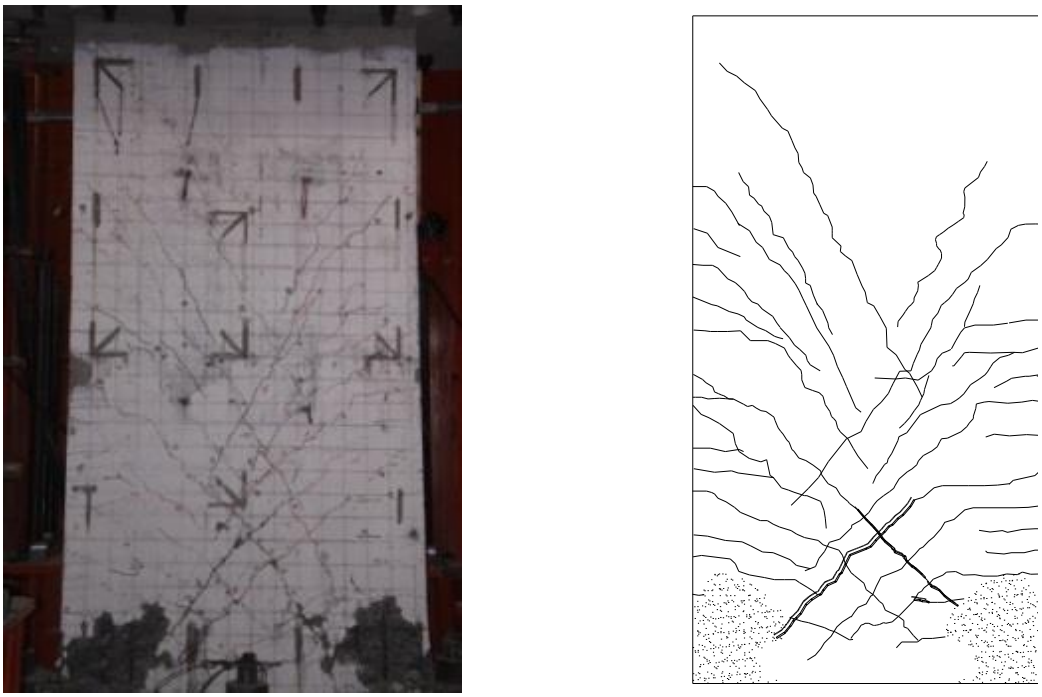

(a) Photo (b) Schematic

Figure 15. Photo and schematic crack patterns of the specimen SW1.

(a) Photo (b) Schematic

Figure 16. Photo and schematic crack patterns of the specimen TW1.

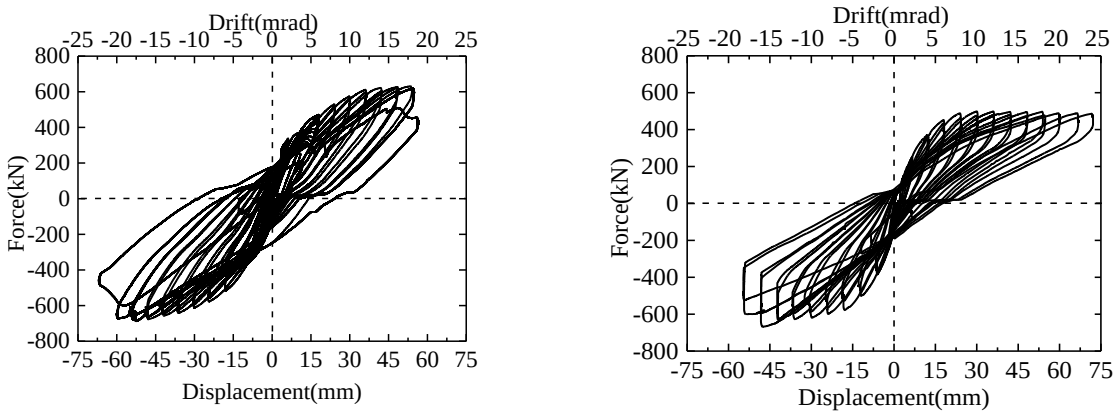

(a) Specimen SW1 (b) Specimen TW1

Figure 17. Hysteretic loops.

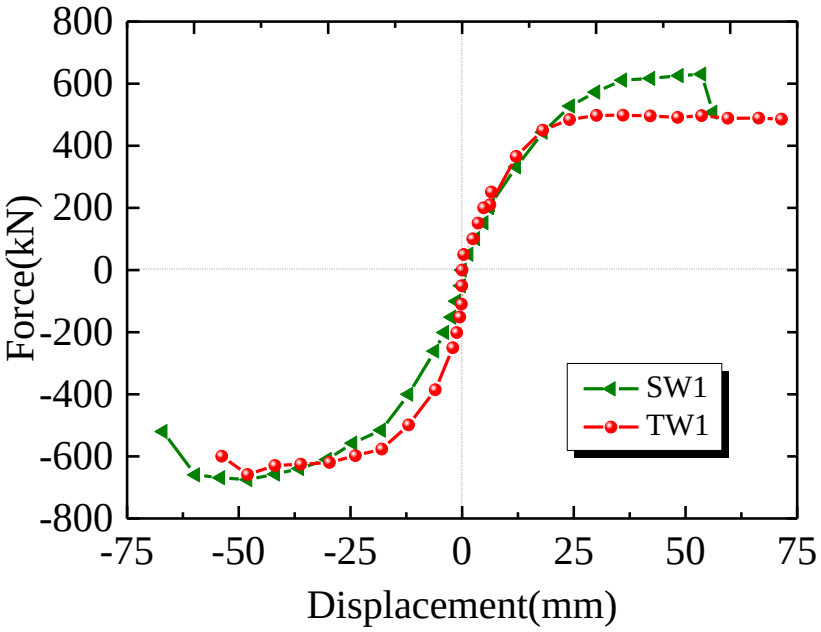

Figure 18. Skeleton curves of specimens SW1 and TW1.

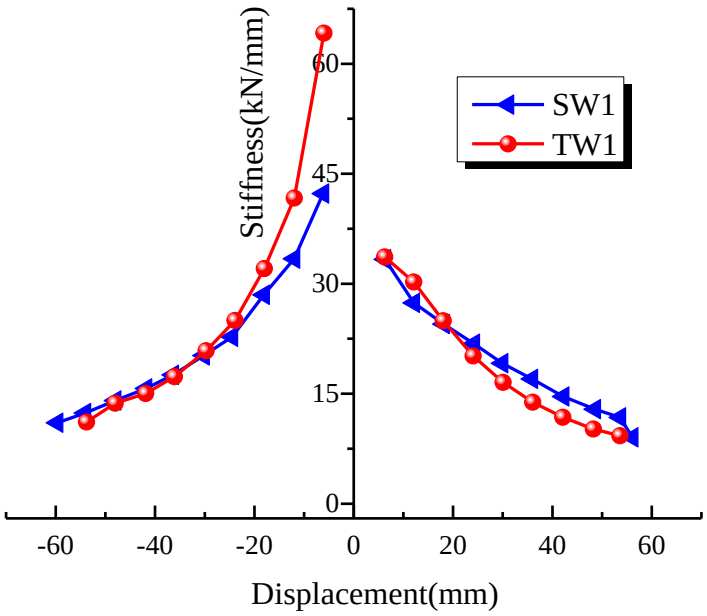

Figure 19. Stiffness degradation curves of specimens SW1 and TW1.

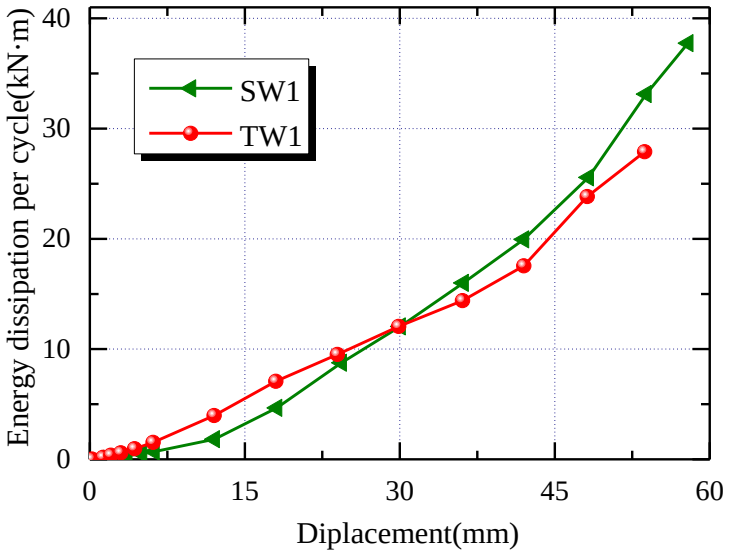

Figure 20. Energy dissipation per cycle for specimens SW1 and TW1.

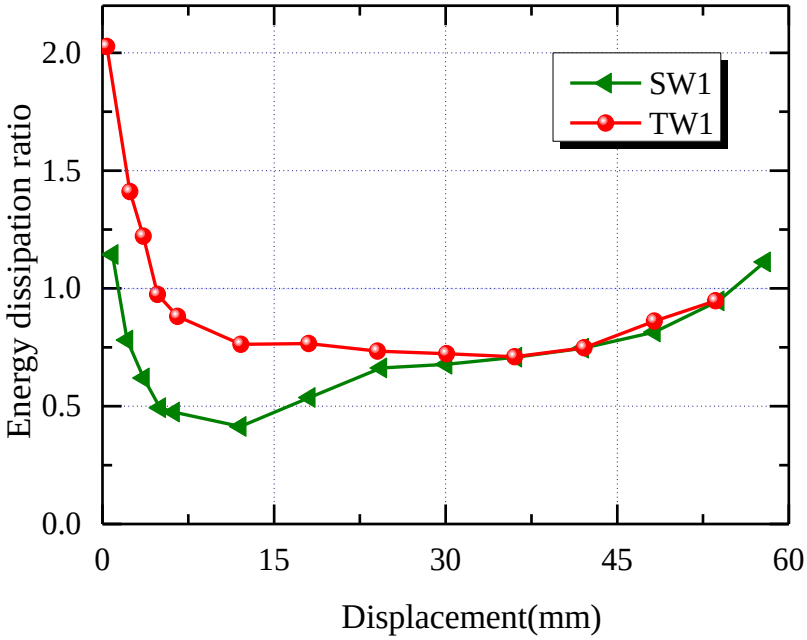

Figure 21. Energy dissipation ratio per cycle for specimens SW1 and TW1.

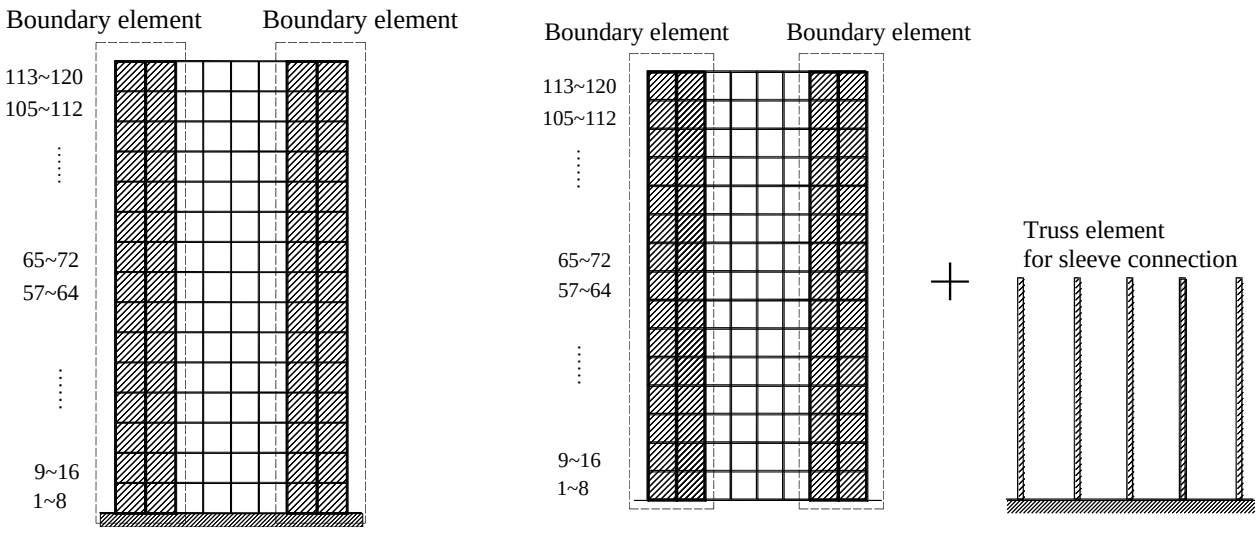

(a) SW1 (b)TW1

Figure 22. FE model of a shear wall.

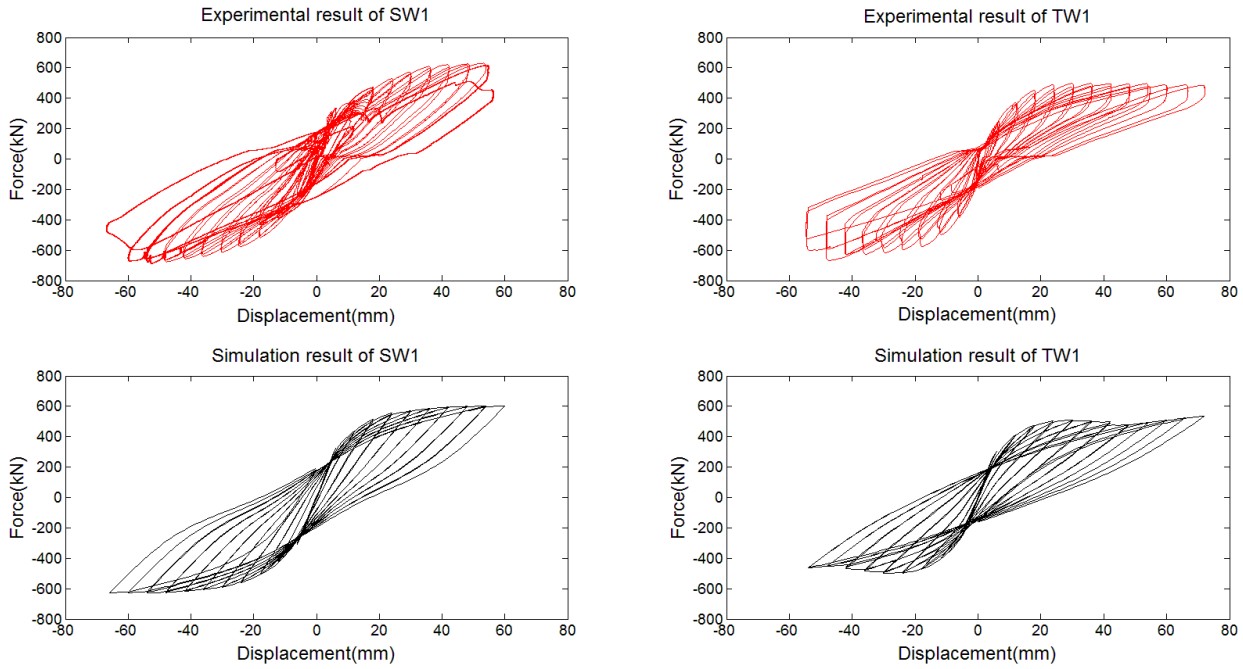

Figure 23. Comparison of hysteretic loops for specimens SW1 and TW1.